



Nanoindentation of ZrH₂ by molecular dynamics simulation

Linyuan Shi (石临源), Michele L. Fullarton, Simon R. Phillpot*

Department of Materials Science and Engineering, University of Florida, Gainesville, FL, 32611, USA



ARTICLE INFO

Article history:

Received 13 February 2020

Received in revised form

2 July 2020

Accepted 8 July 2020

Available online 15 July 2020

ABSTRACT

Classical molecular dynamics simulations of nanoindentation on the (100) and (110) planes using a spherical indenter are performed to investigate the deformation behavior of δ-ZrH₂. The Charged Optimized Many Body (COMB) potential is used to describe the interatomic interactions. The effect of the indenter speed and the thickness of the active layer to the nanoindentation are evaluated. We find that the nucleation and movement of {100} <110> dislocations are the main mechanisms of the inelastic deformation during nanoindentation on both the (100) and (110) planes. In addition, the load-displacement curve, hardness and deformation processes extracted from δ-ZrH₂ nanoindentation on the (100) and (110) planes are analyzed.

© 2020 Elsevier B.V. All rights reserved.

1. Introduction

Pressurized water reactors (PWRs) and boiling water reactors (BWRs) are widely used as commercial nuclear reactors around the world [1]. Because of their low thermal neutron absorption, high corrosion resistance and great mechanical properties, zirconium-based alloys such as Zircaloy [2] and ZIRLO [3] are used as fuel cladding to establish the first barrier in preventing fission products from entering into the primary cooling circuit [4,5]. However, excessive hydrogen generated in the reaction between water and zirconium precipitates as zirconium hydride in the cladding; this can lead to reduction of the fracture toughness and ductility of the clad, ultimately resulting in mechanical failure [6]. Therefore, understanding the deformation behavior of zirconium hydrides will be helpful in improving the design and the performance of the cladding. Many density functional theory (DFT) calculations have been conducted to investigate the ground state properties of the Zr–H system, including the lattice parameter, elastic constants, surface energy, and vacancy and interstitial formation energies [7–9]. Although previous Molecular Dynamics (MD) simulations have focused on the investigation of the hydrogen diffusion in Zr [10], deformation processes in the polycrystalline Zr [11], nanoindentation of the Zr [12] and ZrO₂/Zr [13], there has been little simulation work on the deformation process in ZrH_x.

Nanoindentation has been widely used in experiments to characterize the Young's modulus, yield stress, fracture toughness and deformation process of zirconium hydride at the microscale [14–16]. However, it is still very challenging to observe the nucleation and propagation of dislocations at the atomic scale. Nanoindentation by MD simulation has been widely used to characterize the deformation processes at the atomic scale. For example, Li et al. used nanoindentation simulation to identify the defect nucleation process resulting in hardening in gold and gold alloys [17]. Fu et al. performed nanoindentation simulation on VN(001) films, from which they identified the formation mechanism of dislocation loops and the initial plastic deformation during the indentation [18]. Sun et al. used nanoindentation simulation to explore the formation mechanism of the prismatic loops in the 3C–SiC single crystal [19]. Wang et al. investigated the “double cross” splitting mechanism of single-crystal diamond using nanoindentation simulation [20]. In this work we perform MD simulations of nanoindentation on δ-ZrH₂ with a spherical indenter to characterize the formation mechanism of dislocations at the atomic level. In Section 2, the methods employed in the work, the simulation setup, the structure and the slip system of ZrH₂ are introduced. In Section 3, the influence of the indenter speed and the influence of the thickness of the active layer during the nanoindentation are analyzed. In Section 4, the effects of indentation on the <100> and <110> surface orientations are discussed. The conclusions are in Section 5.

* Corresponding author.

E-mail address: sphil@mse.ufl.edu (S.R. Phillpot).

2. Background and methods

2.1. Interatomic potential

There are MEAM [10], EAM/ALLOY [21] and COMB3 [22,23] interatomic potentials for the Zr–H binary system. The MEAM and EAM/ALLOY potentials were specifically fitted for the simulation of diffusion of hydrogen atoms in hcp α -Zr. As a result, they cannot be expected to give a good description of the hydride. Indeed, both the MEAM and EAM/ALLOY potentials predict the ZrH_x structure to be mechanically unstable, which is contradicted by the experimental observation. By contrast, the COMB3 potential was fitted for Zr–H binary compounds and predicts a stable δ - ZrH_2 structure at 0 K and room temperature. Zhang et al. showed that the COMB3 potential is capable of describing the homogenous hydride formation path in α -Zr and predicts a formation energy for δ - $ZrH_{1.0-2.0}$ which in good agreement with DFT results [24]. The stacking fault energy (SFE) of α -Zr and the ζ hydride were also investigated by Zhang et al. For α -Zr, the stable and unstable SFE were found to be 104 and 134 mJ/m² with the COMB potential. The same properties calculated by DFT calculations [25] were 227 and 285 mJ/m² respectively. For ζ -hydride, a negative stable SFE was predicted by both the COMB potential (-51 mJ/m²) and DFT calculations (-95 mJ/m²). Although the COMB potential underestimates the absolute values of SFEs compared with DFT calculations, the shape of SFE curve is similar with that from previous DFT calculations. We thus expect that the dislocation-related plastic processes predicted by COMB will be consistent with those that would be obtained from ab initio DFT if such simulations were possible and such large systems. While $ZrH_{1.5-1.7}$ is most often observed as the cubic δ -phase, the ground state of stoichiometric ZrH_2 is actually the ϵ -phase, a tetragonally ($c/a = 0.878$) distorted fluorite structure. It was found that COMB3 could not describe both the ϵ - ZrH_2 and δ - ZrH_2 simultaneously; it was therefore parameterized to the δ -phase only, with the intent that ϵ -phase compositions be approximated as the δ -phase. Therefore, in this work the nanoindentation simulations on the stoichiometric composition use the cubic structure δ - ZrH_2 . Table 1 lists the lattice parameter and elastic moduli of δ - ZrH_2 calculated by COMB3 potential. The lattice parameter and bulk modulus, B , agree well with DFT values. However, the individual elastic constants contributing to $B = (1/3)(C_{11} + 2C_{12})$ do not agree well with the DFT values. DFT calculations yield low, or in one case negative, values for C_{44} and the shear constant, $G = (1/2)(C_{11} - C_{12})$, indicating the zero-temperature instability of stoichiometric δ - ZrH_2 . Mechanical stability is ensured in MD simulations of δ - ZrH_2 by the parameterization of COMB3 potential. Since we are primarily interested in plastic events, particularly those associated with dislocations, the SFE is more important than the elastic constants: errors in the elastic constants can be expected to change the values of the stresses needed for plastic events to take place but should not change the deformation mechanisms. We conclude that although clearly imperfect, the COMB3 potentials offers a physically reasonable description of δ - ZrH_2 . We will revisit the issue of the

fidelity of the COMB3 potential when we compare the nanoindentation simulations with experimental results.

2.2. Simulation setup

The MD nanoindentation simulations were performed using the LAMMPS code [27]. As shown in the Fig. 1, the nanoindentation simulation cell consists of three regions: a top, active region, which is indented; a middle, thermostat region, responsible for temperature control; and a bottom, fixed region, in which the atom positions do not move, thereby providing the rigid support for the indentation process. There is also a 150 Å vacuum layer above the top surface of the active layer to provide space for the spherical indenter. This spherical indenter is a non-atomic repulsive sphere which exerts forces on the atoms in the active layer according to the equation (1):

$$F(r) = -K(r - R)^2 \quad (1)$$

In equation (1), F is the repulsive force on each atom, $K = 10$ eV/Å² is the specified force constant, r is the distance from the atom to the center of the indenter, and R is the radius of the indenter, which is set as 45 Å in the all MD simulations in this work. The force is zero if $r \geq R$. A Langevin thermostat [28] is applied to the thermostat layer, thereby maintaining the temperature of the whole system at a relatively constant value; as a result, in our simulations there is no systematic increase in temperature despite the large amount of work done on the system by the indenter. The thicknesses of the thermostat and fixed layers are 90 Å and 10 Å respectively in all simulations; the effect of the choice of thickness of the active layer is discussed below. The length of the square edges of the simulation cell in the x-y plane is set to 200 Å. This is more than twice larger than the diameter of the indenter, thereby providing a region of undeformed material around the indent. Periodic boundary

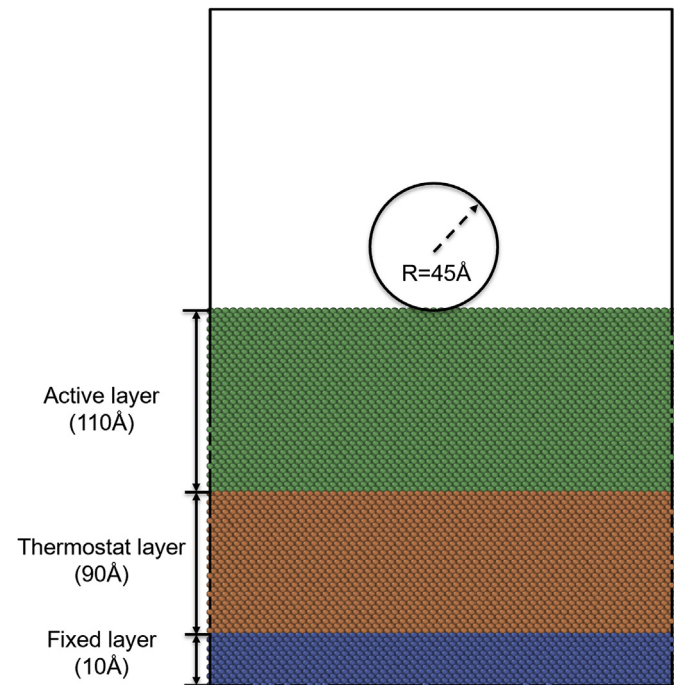


Fig. 1. Sketch of the simulation system. Active layer, thermostat layer and fixed layer are colored as green, orange and blue, respectively. Only Zr atoms are shown in this figure. (For interpretation of the references to color in this figure legend, the reader is referred to the Web version of this article.)

Table 1

Lattice parameter, elastic constants, and moduli of cubic fluorite ZrH_2 calculated by DFT and COMB3 potential.

	DFT [7]	DFT [26]	COMB3(this work)
$a(\text{\AA})$	4.82	4.87	4.91
$C_{11}(\text{GPa})$	83	101	364
$C_{12}(\text{GPa})$	160	119	21
$C_{44}(\text{GPa})$	-20	34	48
$B(\text{GPa})$	133	113	135
$G(\text{GPa})$	-27	17	170

conditions are applied in the plane. Before the indentation simulation, the whole system is equilibrated at 300 K for 10 ps with an integration time step of 1 fs. Charge equilibration in conjunction with the COMB3 potential is performed throughout the entire simulation. The ratio of the indentation depth to the radius of the indenter is intended to minimize pile-up effects [29], in which atoms near the indenter are pushed up above the contact surface. Thus, the maximum indentation depth is set to 25 Å in all simulations to reduce the impact such pile-up effects. The Ovito [30] software tool is used to visualize and analyze the MD simulation result.

2.3. Structure and slip system

There are three zirconium hydride ZrH_x phases reported in past investigations in zircalloy: the metastable γ -phase (fct, $c/a > 1$), the δ -phase with face centered cubic(fcc) structure, and the ϵ -phase with face centered tetragonal structure (fct, $c/a < 1$) [31]. The γ , δ and ϵ phases have similar crystal structures and decreasing c/a ratio with increasing hydrogen concentration. DFT calculations show the energy difference between the fcc structured δ - ZrH_2 and ϵ - ZrH_2 to be only +7meV/atom [8] and thus fct ϵ - ZrH_2 is more stable. For ϵ - ZrH_2 , $c/a = 0.878$ [25], whereas for δ - ZrH_2 $c/a = 1$. Although this fcc structure is predicted unstable due to the negative G and C_{44} values in Table 1 by DFT calculation, the mechanical stability is ensured by the COMB3 potential by meeting the following stability conditions for cubic systems:

$$C_{11} > 0, C_{44} > 0, C_{11} > |C_{12}|, (C_{11} + 2C_{12}) > 0 \quad (2)$$

The energy difference between fct ϵ - ZrH_2 and δ - ZrH_2 is +13meV/atom in COMB potential and is -7meV/atom in DFT calculations; as a result, the fct ϵ - ZrH_2 transforms to fcc δ - ZrH_2 after energy minimization using COMB potential. We note that kT at room temperature is 25meV/atom; thus, all of these energy differences are very small. For this reason, and because δ - ZrH_2 is the most widely observed phase in fuel cladding, the fluorite fcc structure, δ - ZrH_2 , is used in the simulation in place of ϵ - ZrH_2 . The [100] and [110] orientations were chosen in our simulations to investigate the anisotropy of δ - ZrH_2 . For convenience in the simulation, a body centered tetragonal unit cell, shown in Fig. 2(a), is used, oriented along the [110], [110] and [100] lattice directions. The relationship between the conventional cubic unit cell and the body centered tetragonal unit cell is illustrated by a supercell of δ - ZrH_2 in Fig. 2(b). This bct unit cell contains both (100) and (110) planes. Indentation at different orientations is achieved by choosing different planes of this bct unit cell. Nanoindentation on the (100) and (110) planes will be studied in this work.

δ - ZrH_2 has a fluorite like structure where Zr atoms occupy the Bravais lattice sites of fcc cubic sublattice and H occupies all the tetrahedral interstitial sites. Experiments on fluorite structures CaF_2 [32] show that it has a {100}<011> primary slip system. There are three orthogonal {100} plane in the fluorite structure. Each plane has two orthogonal <110> slip directions. Therefore, the fluorite structure has six unique slip plane-direction possibilities.

2.4. Theory and analysis method

2.4.1. Hertz theory

The force vs. indentation depth curves are obtained from nanoindentation simulations performed in LAMMPS. As will be shown in Section 3, the deformation shows an elastic response before the first plastic event. Therefore, Hertz theory [33,34], based on contact mechanics, is used to analyze the elastic deformation behaviors in our simulations:

$$P = \frac{4}{3} E^* R^{\frac{1}{2}} h^{\frac{3}{2}} \quad (3)$$

where P is the load on the indenter, R is the radius of the spherical indenter and h is the indenter depth. The reduced Young's modulus, E^* , is :

$$E^* = \left\{ \frac{1 - \nu_s^2}{E_s} + \frac{1 - \nu_i^2}{E_i} \right\}^{-1} \quad (4)$$

where E_s and ν_s and E_i and ν_i are Young's moduli and Poisson ratios of the sample and indenter respectively. In this work, the force field indenter is treated as an ideal hard indenter with $E_i = \infty$ and $\nu_i = 0$. Thus $E^* = E_s/(1 - \nu_s^2)$.

The hardness, H , can also be extracted from nanoindentation simulations and compared with the prediction of Hertz Law:

$$H = \frac{P}{A} \quad (5)$$

where A is the contact area between the indenter and the surface of the sample. The contact area A is given by

$$A = \pi h(2R - h) \quad (6)$$

where h is the indentation depth and R is the radius of the spherical indenter. In this work, we calculate Young's modulus and Poisson's ratio for the (100) and (110) surfaces independently by Hertz Law. The values of Young's modulus, Poisson's ratio and reduced Young's modulus, computed by the elastic constants are shown in Table 2

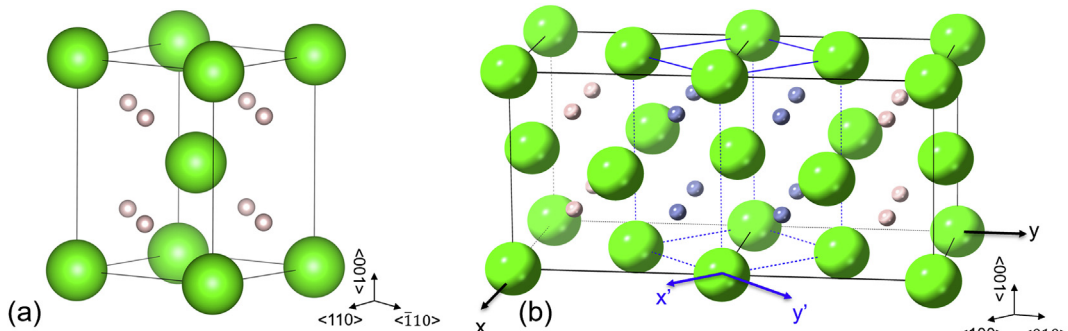


Fig. 2. (a) Body centered tetragonal unit cell of δ - ZrH_2 structure. (b) A supercell of δ - ZrH_2 to illustrate the relationship of the conventional cubic unit cell and body centered tetragonal unit cell where hydrogen atoms in the tetragonal unit cell are colored as blue Zr atoms are green, H atoms are grey. (For interpretation of the references to color in this figure legend, the reader is referred to the Web version of this article.)

Table 2

Young's modulus, Poisson's ratio and reduced Young's modulus of $\delta\text{-ZrH}_2$ in the [100] and [110] orientations obtained from the COMB3 potential.

	E_s (Gpa)	ν_s	E^* (Gpa)
[100]	361	0.055	362
[110]	167	0.592	257

and are used in contact mechanics calculation for the (100) and (110) surfaces. For isotropic materials, the Poisson's ratio should be within the bounds -1 to 0.5. However, because of the anisotropy of ZrH_2 , the Poisson's ratio is different at various directions and it can be negative or larger than 0.5 at the specific direction. It is worth noting that the Poisson's ratio on the (110) surface is larger than 0.5, which is measured at the measurement direction [01̄1] and stretched direction [011]. Cubic materials can have positive values larger than 0.5 at this facial diagonal direction such as RbBr (0.64), KI (0.61) and ReO_3 (0.59); or negative values such as Li (-0.52), CuAlNi (-0.65) [35–38]. Therefore, it is possible that ZrH_2 has a Poisson's ratio larger than 0.5 at direction [01̄1]. For comparison, the Poisson's ratio ν_0 in the [100] direction was determined in a by previous DFT calculation [7] to be 0.397, whereas COMB yields 0.055. The difference between COMB and DFT results of Poisson's ratios is a direct result of the overestimation of C_{11} and underestimation of C_{12} , which will be discussed in the section 3.2. The relationship between loads from two different indentation scenarios with different indenter radii and depth for the same material can be expressed as

$$\frac{P_1}{P_2} = \sqrt{\frac{R_1}{R_2}} \left(\frac{h_1}{h_2} \right)^{\frac{3}{2}} \quad (7)$$

where P_1 and P_2 are the loads, h_1 and h_2 are indentation depths. To connect the simulations to experiment, the experimental results, which are on μN scale, will be scaled to the $n\text{N}$ -scale simulations according to equation (7).

2.4.2. Local atomic symmetry analysis

The Central Symmetry Parameter (CSP) [39], widely used to characterize the symmetry breaking in an atom's local environment, can indicate the degree of disorder in the region of the deformation, especially for bcc and fcc structures. Therefore, we characterize the local disorder degree of atoms during indentation by the CSP value. Because Zr atoms are located on the fcc sublattice in $\delta\text{-ZrH}_2$, the CSP value is also useful to characterize the local disorder of Zr atoms in this work. The CSP for any given atom is defined by equation (8):

$$\text{CSP} = \sum_{i=1}^{\frac{N}{2}} \left| \mathbf{R}_i + \mathbf{R}_{i+\frac{N}{2}} \right|^2 \quad (8)$$

where N is the number of the nearest neighbors of one atom, \mathbf{R}_i and $\mathbf{R}_{i+\frac{N}{2}}$ are the vectors from the central atom to a pair of nearest

neighbor atoms which has the smallest value of $\left| \mathbf{R}_i + \mathbf{R}_{i+\frac{N}{2}} \right|$. As a

result, The CSP is zero for an atom located on a lattice site in a perfect symmetric crystal structure such as bcc or fcc. If there is a vacancy or an interstitial atom in the lattice, then the CSP value of the atoms in the vicinity of the defect will be not zero. Also, the CSP value of the atoms located in an inhomogeneously distorted lattice will be non-zero. Therefore, the CSP value represents the degree of

symmetry breaking in the lattice. Because fcc structure has 12 nearest atoms respectively, the value of N is set to 12.

3. Analysis of loading and unloading

Nanoindentation is a well-established technique to investigate the time-dependent deformation behavior and mechanical properties of a small sample of material. Nanoindentation by MD simulation makes it possible to characterize the nucleation and growth of dislocations at an atomic scale. During the loading process, the force applied on the indenter gradually increases as the indenter moves deeper into the sample. The load vs. displacement curve should match the solution of elastic contact mechanics developed by Hertz [40] before any sudden drop in the load curve. The point where the sudden load drop occurs is often referred as the yield point in the nanoindentation; One phenomenon that is sometimes observed in experiments is a sudden displacement burst of the indenter represented as a plateau in the load vs. displacement curve; this is often referred to as pop-in behavior. If the force follows a 3/2 power rule with indenter depth before the yield point, according to the equation (3) the loading is considered as elastic. The load and unload force vs. depth curve will be identical in the elastic region. Both experiments [41–43] and MD simulations [18,19,44] observed the nucleation of the dislocations at the yield point, which associates the elastic-plastic transition with pop-in. However, nanoindentation experiments on aluminum [45] also show that it is possible for there to be some plasticity or nucleation of the dislocation before the pop-in during indentation, i.e., while the material still displays elastic-like behavior. The indentation simulation could also be affected by factors such as the speed of the indenter and the size of the thin film. Therefore, we will discuss the influences of these factors, Hertz law and hardness in this section. The relations between yield point and dislocations will be discussed in section 4.

3.1. The effect of indenter speed and active layer thickness

The system dimensions in these MD simulations are of the order of 100 Å. We anticipate that the indentation simulation result may be influenced by factors such as the thickness of the active layers and the speed of the indenter. In order to investigate the influence of these factors, we varied both the velocity of indenter and the thickness of the layers. Although the loading rates of 25–50 ms⁻¹ in the simulations are much faster than experiments, which ranges from nm s⁻¹ to 1 mm s⁻¹ [46], they are similar to the indentation rates in other MD simulations [13,17,18,47]. Although this indentation speed is high, all of the processes seen in the simulation are at speeds below the sound speed 2517 ms⁻¹ [9] and are thus, to a large extent, capturing the same physics as would be captured by very slow speed simulations. It can be clearly seen in Fig. 3(a) that the load-displacement curves are essentially the same at the two speeds. Therefore, to improve the simulation efficiency, 50 ms⁻¹ is selected as the velocity of the indenter for the following simulations.

To investigate the influence of the thickness of the active layer, we simulated several nanoindentations with thicknesses of the active layer ranging from 30 Å to 130 Å on both the (100) and (110) planes. Fig. 3(b–c) shows that the thickness of the active layer affects the load vs. displacement curve. It can be clearly seen in Fig. 3(b) that with an increase of the thickness of the active layer, the load is slightly lower, especially for small thicknesses. As the active layer thickness is small, the so-called substrate effect [48] is obvious. The influence due to stiffness of the presence of the fixed layer cannot be neglected. When the total thickness is larger, the substrate effect is weaker. Therefore, the influence of the thickness

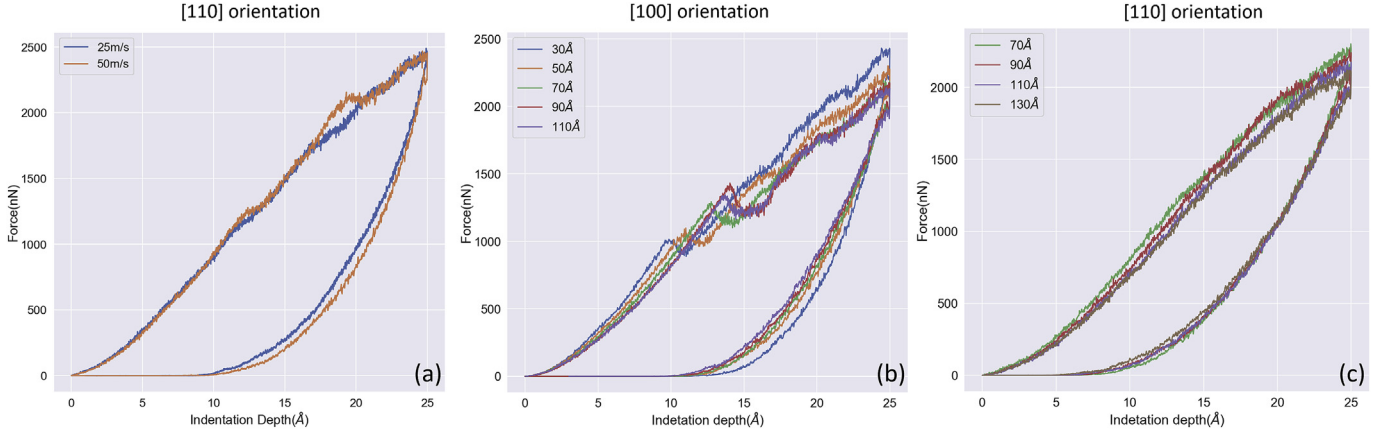


Fig. 3. (a) Force vs. indentation depth curves for $\delta\text{-ZrH}_2$ nanoindentation simulation on the (110) surface at two different speeds with the active layer thickness of 60 Å. (b–c) Force vs. indentation depth curve for active layers of various thicknesses during nanoindentation simulations on the (100) and (110) surfaces respectively.

of the different active layers can be ascribed to the substrate effects. For the indentation on the (100) plane this thickness is ~ 90 Å; for the indentation on the (110) plane it is a little larger, ~ 110 Å. For all thicknesses, however, the indentation curves have the same general shape. Fig. 3(b) shows that the force and indentation depth for the first plastic event on the (100) plane does increase with increasing thickness; however, the difference between the 90 Å and 110 Å thicknesses is small, indicating that the asymptotic regime has been reached. These changes in the load-displacement curve's shape with active layer's thickness is most likely caused by the rigidity of the lower fixed layer. The deferred plastic event on thicker active layers indicates that the simulation cell shows more elastic behavior than with smaller thickness active layers. For a thicker active layer, the dislocations have more space to grow before interacting with the atoms in fixed layer. In addition, it seems that this rigid layer prevents their transmission and results in a stress in the system that tends to impede further plasticity events. For indentation on the (110) plane, because no noticeable force drop is found in the load-displacement curve, we don't find a similarly impeded plastic deformation (see Fig. 3(c)). As for the dislocations themselves, their structures appear to be independent of the thickness of the active layer. Therefore, the nanoindentation simulations with thickness 110 Å and 130 Å are selected for dislocation analysis in the following sections for the (100) and (110) planes respectively. Similar substrate effect was also seen in the nano-indentation simulations of Zr and Ni [12,49].

3.2. Hertz law and hardness

Before the first plastic deformation occurs, the mechanical response during the simulation should be elastic. Therefore, the MD simulation results should be consistent with Hertz analysis. From equation (3), the force should be linear in $h^{\frac{3}{2}}$. Fig. 4 shows the load is indeed linear with the $h^{\frac{3}{2}}$ for both orientations and all different thicknesses. The reduced Young's modulus fitted by the linear regression of each curve is shown in Table 3 for both (100) and (110) planes. Interestingly, the (100) plane on the 30 Å system gives an elastic response that matches Hertz Law while the 110 Å thickness, which we expect to be more physically realistic, is softer than the Hertz Law prediction. The curve for the 110 Å active layer thickness for indentation on the (110) plane matches well with the prediction of Hertz theory. These trends are similar to those seen in nanoindentation simulations of Zr and ZrO_2 [12,13], where the load-displacement curve for nanoindentation on the Zr (0001)

surface is steeper than the Hertz law predictions, while load-displacement curve obtained for the ZrO_2/Zr (110)/(100) surface is softer than the Hertz law predictions. We attribute the deviation between the simulations and the Hertz prediction to the simulation system size. Overall, despite these quantitative differences, the load-displacement curves are consistent with the Hertz Law predictions.

Now we examine the hardness vs. depth curve. Both curves for the [100] and [110] orientations in Fig. 5 show that the hardness curve levels off at about 40 GPa when the indentation depth reaches 15 Å. Interestingly, unlike the elastic properties, there is not a significant dependence of the hardness on the thickness of the active layers. The reported experimental value for the hardness of ZrH_2 is 3–4 GPa [50]. Although the hardness of a material is mainly related to the plastic property of materials, both elastic deformation and plastic deformation contribute to the hardness [51,52]. The large difference between the predicted and experimental hardnesses is mainly caused by the differences in the experimental and COMB3 elastic constants. The COMB3 potential overestimates the C_{11} value and underestimates the Poisson's ratio in the [100] orientation, which results in the overestimation of reduced Young's modulus. The reduced Young's modulus of the $\delta\text{-ZrH}_2$ for the (100) surface is 362 GPa, compared with the value predicted by DFT of 53 GPa. To remove the influence of the overestimate of reduced Young's modulus, dimensionless load (P/E^*) and dimensionless hardness (H/E^*) are calculated and showed in Fig. 6. Indentation experiment results [14] are also plotted in Fig. 6 for comparison after rescaling the load and indenter size according to Equation (7). As Fig. 6 shows, the overall dimensionless load vs. depth curve of simulation match well with the experiments. In addition, the dimensionless hardness extracted from the indentation simulation has similar trends and is at the same level as the experimental value. Despite these quantitative differences, the overestimation of the hardness is unlikely to significantly modify the dislocation processes present in the nanoindentation simulation.

4. Atomic-level mechanisms

4.1. Nanoindentation on the (100) surface

Fig. 7 (a) shows the load-displacement curve for the nano-indentation simulation on the (100) $\delta\text{-ZrH}_2$ plane. The first load drop occurs at an indentation of 13.6 Å, which represents the yield point. Fig. 7(b) shows the sum of CSP values of the atoms vs. indentation depth of nanoindentation on the (100) $\delta\text{-ZrH}_2$ plane.

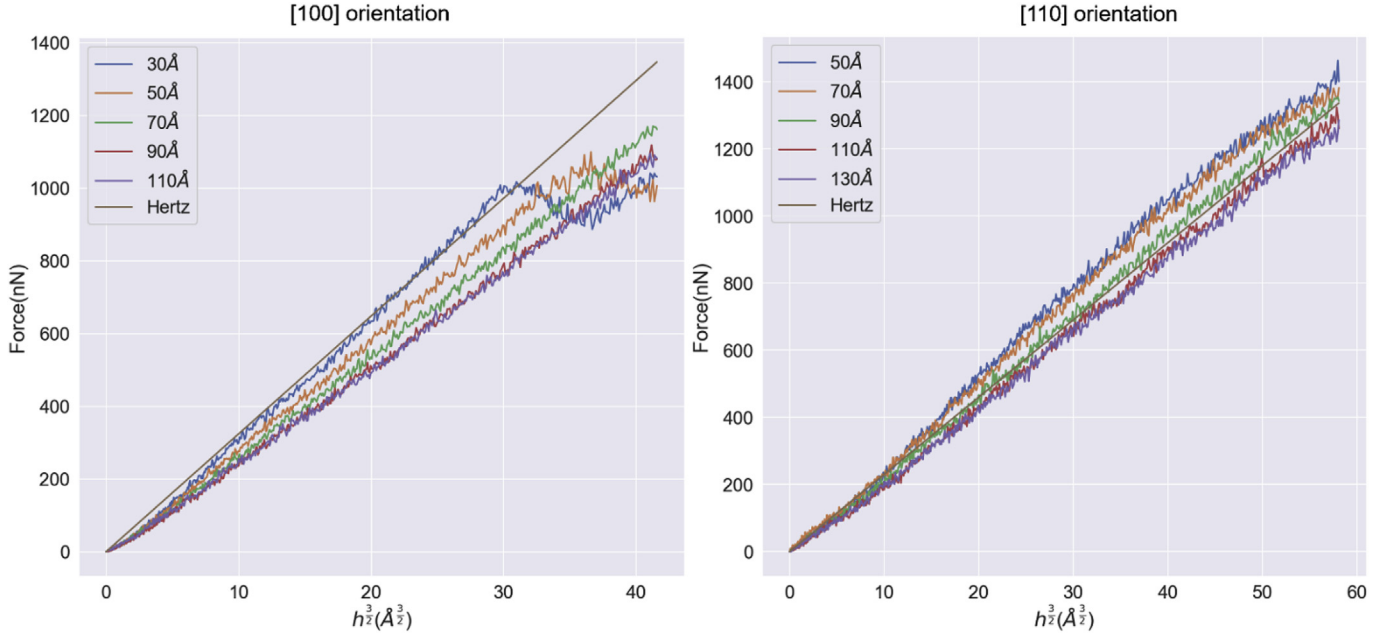


Fig. 4. Force vs. $h^{3/2}$ for active layers of different thickness ranging from 30 Å to 130 Å during nanoindentation simulations on the (100) and (110) planes respectively. The predictions of Hertz theory are also shown.

Table 3

The fitted reduced Young's modulus of δ -ZrH₂ obtained from the load vs. force curves of various thickness of active layers in the [100] and [110] orientations.

Active layer thickness(Å)	E^* in [100] orientation (Gpa)	E^* in [110] orientation (Gpa)
30	371	N/A
50	334	287
70	316	278
90	297	267
110	292	255
130	N/A	248

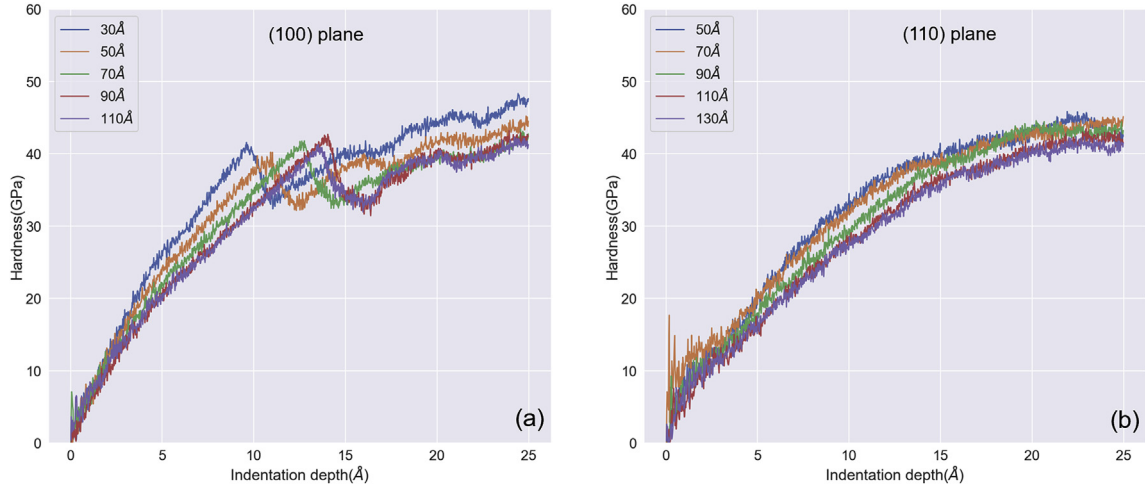


Fig. 5. Hardness vs. indentation depth with active layers of different thickness ranging from 30 Å to 130 Å during nanoindentation simulation on the (100) and (110) planes respectively.

Fig. 7(c)–(f) show atomic-level processes that take place during indentation. Only the Zr atoms are shown, colored by their CSP value, showing only those with CSP values larger than 3, i.e., those in environments significantly different from perfect fcc. We thus

only see atoms at the surface (red atoms) and those atoms that are part of the structure developed during the plastic deformation. As the depth of the indent increases, the amount of disorder in the system increases and the total sum of the CSP values increases. The

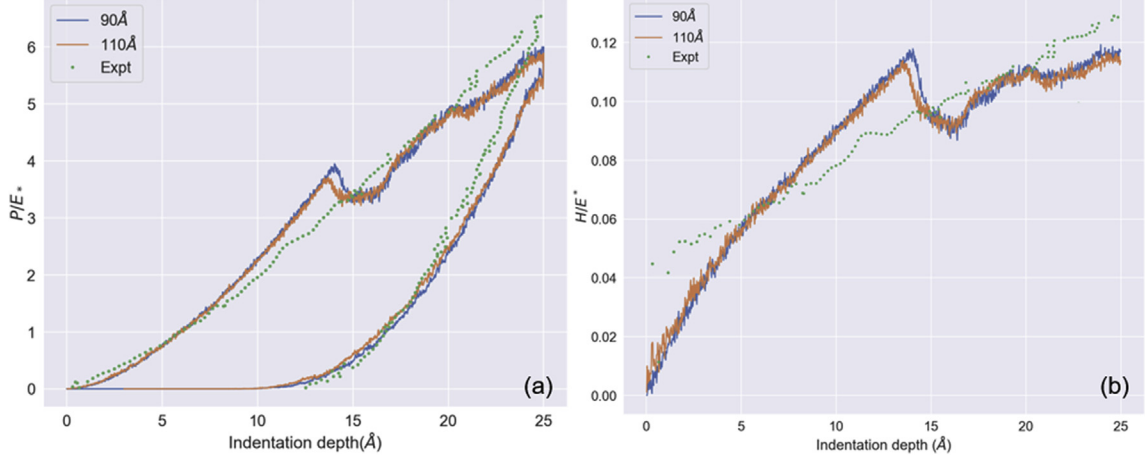


Fig. 6. (a) Dimensionless load vs. indentation depth (b) Dimensionless hardness vs. indentation depth for (100) plane extracted from simulations and experiment.

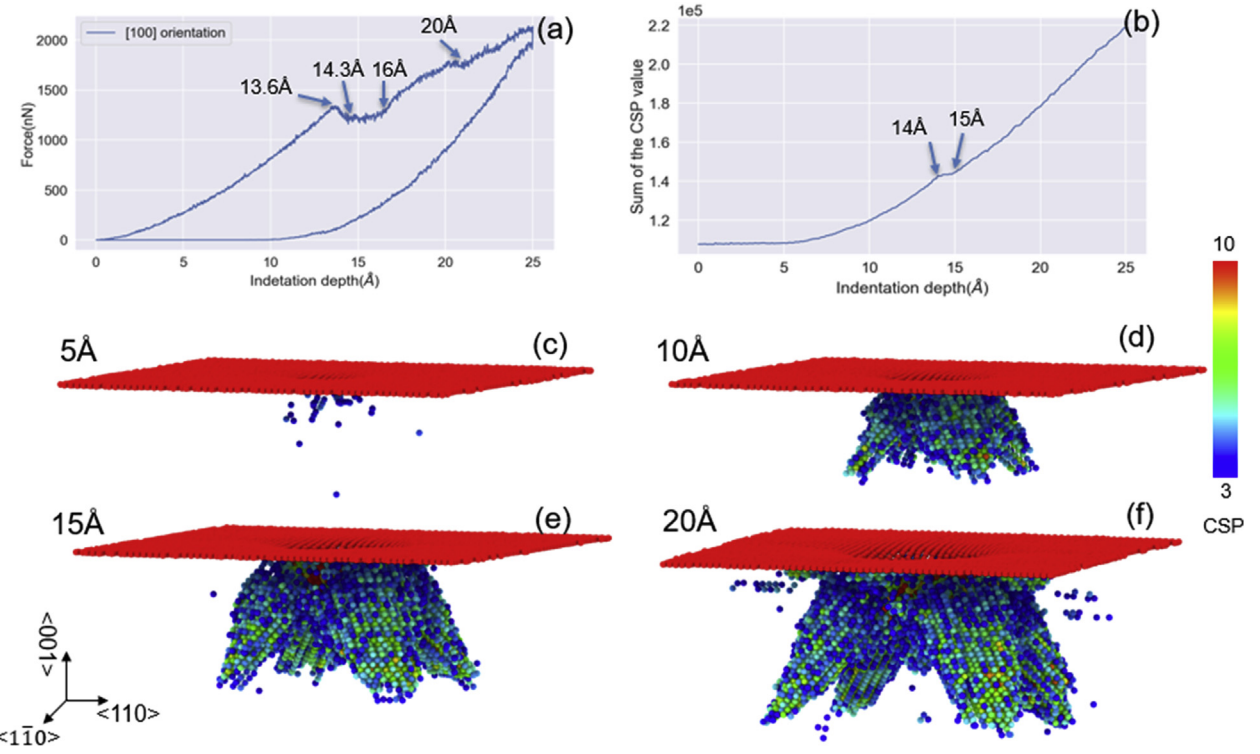


Fig. 7. (a) The load-displacement curve of the nanoindentation simulation on the (100) δ -ZrH₂ plane. (b) The sum of CSP values of the atoms vs. indentation depth of nano-indentation on the (100) δ -ZrH₂ plane. (Only atoms of which $CSP > 3$ are counted) (c–f) The snapshots of microstructure evolution at different indentation depth during nano-indentation simulation on the (100) δ -ZrH₂ plane.

CSP value begins to significantly increase after only 5 Å of indentation, Fig. 7(b). After the first load drop occurs, at 13.6 Å, the increase in the sum of CSP values slows down at 14 Å indicating dislocation propagation and nucleation.

Fig. 7(c–f) show the evolution of the microstructure during nanoindentation on the (100) plane. Fig. 7 (c) clearly shows some plasticity begins at an indentation depth of 10 Å, i.e., before the yield point. This phenomenon, in which non-uniform deformation occurs prior to the yield point but the system still has elastic-like loading, is called pseudo-Hertzian behavior [53] and has been observed previously. Kiely [54] et al. observed some minor events consisting of the nucleation of dislocation loops occurred prior to

the pop in during the nanoindentation on pristine gold (111) surface. Minor et al. [45] found the onset of plasticity before the load-drop behavior from in-situ TEM nanoindentation on Al grains and attributed it as the dislocation strengthening caused by the dimensional confinement. Salehinia et al. [55] shows that dislocations may nucleate prior to the yield point with defects in the vicinity of the nanoindentation on Ni with MD. Michael [53] et al. concluded this plastic behavior prior to the yield point is most likely the result of mobile defects in the stressed volume, an uneven surface being flattened (not relevant in simulations) or the presences of vacancies near the vicinity of the indent.

In this work, all simulations are performed at 300 K. A few Zr

atoms may still deviate from the perfect FCC sublattice sites in the system after the equilibration because of the thermal motion and have large CSP values. Additionally, moderate temperatures, such as 300 K, can accelerate the nucleation and dislocation motion. Both these slightly disordered atoms and temperature may contribute to the plasticity before the yield point and to the pseudo-Hertzian behavior. Disregarding the surface atoms, the atoms shown in Fig. 7(c) have a CSP value slightly larger than their neighbors, indicating that dislocations have started to nucleate. With increased indentation depth, the dislocations gradually grow and move to the periodic edge of the simulation cell. Fig. 7(d)–(f) show that four distinct dislocations grow along $\langle 110 \rangle$ directions. Because the x-axis and y-axis both belong to $\langle 110 \rangle$ direction family, these dislocations are symmetric in the x-y plane. Thus, all of these dislocations are of the $\{100\} \langle 110 \rangle$ type.

To further investigate the pseudo-Hertzian behavior, nanoindentations on the (100) δ -ZrH₂ plane with indentation depths of 3 Å, 6 Å, 10 Å and 14 Å were simulated. As shown in Fig. 8(a), the load-displacement curve during the loading and unloading process for indentation depth 3 Å are almost identical indicating that no plasticity occurred during the simulation. For indentation depth 6 Å, which is slightly over the nucleation point of 5 Å, the force on indenter during unloading is slight smaller than during loading. When increasing the total indentation depth, the difference of the force between loading and unloading increases and the enclosed area of the load-displacement curve increases. Fig. 8(b–d) shows the final microstructure of the δ -ZrH₂ when the indenter finished the unloading process and was no longer in contact with the δ -ZrH₂ (100) surface. For the total indentation depth 3 Å, Fig. 9(b), no dislocation is found after unloading, which indicates δ -ZrH₂ has an elastic response during the whole nanoindentation process. However, for the total indentation depths of 6 Å and 10 Å, obvious dislocations are observed after unloading, as shown in the Fig. 8(c) and (d), which indicate the plasticity occurs during the nano-indentation and is irreversible.

The load vs. depth curve for the [100] orientation in Fig. 7(a) shows that the first drop in load occurs at an indentation depth of 13.6 Å. Originally, Zr atoms sit on an fcc sublattice in the δ -ZrH₂ and thus have 12 coordination neighbors. During nanoindentation there is a highly deformed region, with 13–16 coordinated atoms,

near the indenter, just beneath the surface at the indentation depth of 13.6 Å, colored as red in Fig. 9(a–b). The xz-(100) and xz-(010) sliced planes at the center of the indenter are presented in Fig. 9(g–i). The atoms indicated in the circle at the xz-(010) plane in Fig. 9(b) show that the atoms of the highly deformed region move to a closed packed structure with ABAB stacking in the (010) direction. Thus, the highly deformed region can be regarded as a closed packed structure with ABAB stacking during nano-indentation between the dislocation nucleation occurring at 5 Å indentation depth to 13.6 Å. A similar transformation was also observed in nanoindentation simulations of ZrO₂ by Lu et al. [13]. In contrast to the ZrO₂ simulation, in which O atoms were squeezed to away from the Zr atoms, the hydrogen sublattice does not change during the indentation of δ -ZrH₂ from depth 5 Å to 13.6 Å, except in the highly deformed region, presumably because H atoms are very small in comparison to O atoms, which are larger than Zr atoms. Fig. 9(c) shows the H atoms still in a simple cubic sublattice with only minor distortions at depth 13.6 Å. Thus, although the Zr sublattice is distorted and transformed from fcc to ABAB stacking, the H atoms still have enough space to remain in their original tetrahedral interstitial sites.

The empirical covalent radii of H and O are 37pm and 73pm respectively. Based on the lattice parameters of δ -ZrH₂ and ZrO₂, the ratio of the size of the H/O sitting in the tetrahedral vacancy sites to the size of tetrahedron vacancy in ZrH₂ and ZrO₂ fcc lattice are 4.3% and 29.8% respectively, calculated by the equation $(4r^3)/(3V_{tetra})$, where r is the radius of H/O atom and V_{tetra} is the size of the tetragonal site. In addition, because H atoms are small, the lattice parameter of δ -ZrH₂ is mainly determined by the size of the Zr atoms, while the lattice parameter of ZrO₂ is mainly determined by the size of oxygen atoms. As a result, oxygen atoms occupy a larger space in the fcc lattice than the hydrogen atoms, accounting for the smaller distortion seen in the H sublattice compared to the O sublattice during nanoindentation simulations.

The first load drop stops at an indentation depth of 14.3 Å, Fig. 7(a), at which the Zr atoms in the highly deformed region become so disordered that they can no longer maintain ABAB closed packing. Comparing Fig. 9(d) with Fig. 9(a), the highly deformed region shrank from a rectangle to a triangle in the (100) plane. The atoms within the triangle in Fig. 9 (b) have lower

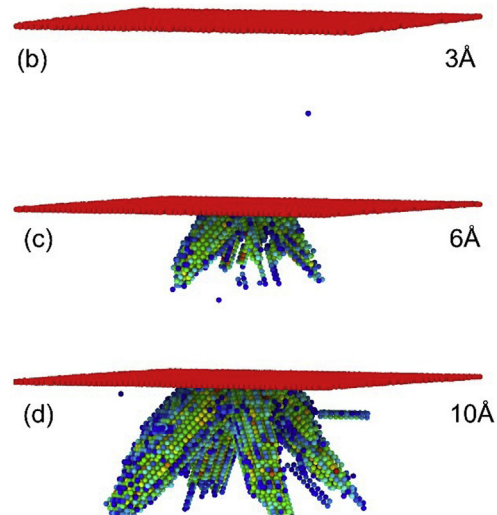
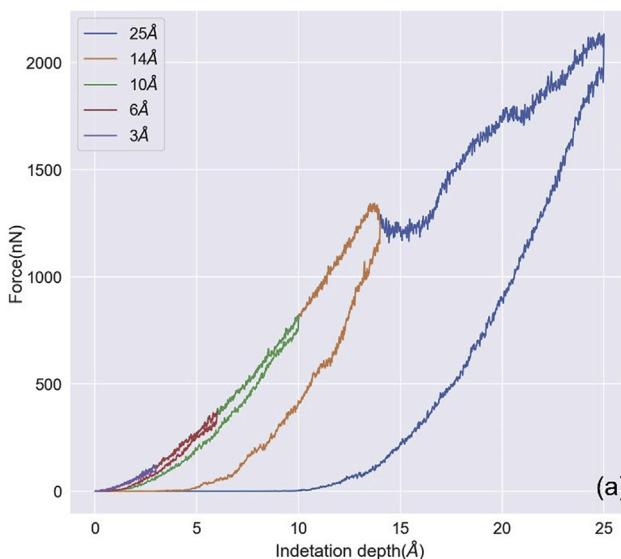


Fig. 8. (a) The load-displacement curve of the nanoindentation simulation on the (100) δ -ZrH₂ plane with indentation depths of 3 Å, 6 Å, 10 Å, 14 Å and 25 Å.(b–d) Snapshots of the final microstructure after unloading from indentation depths of 3 Å, 6 Å and 10 Å respectively. (Only Zr atoms of which CSP > 3 are shown).

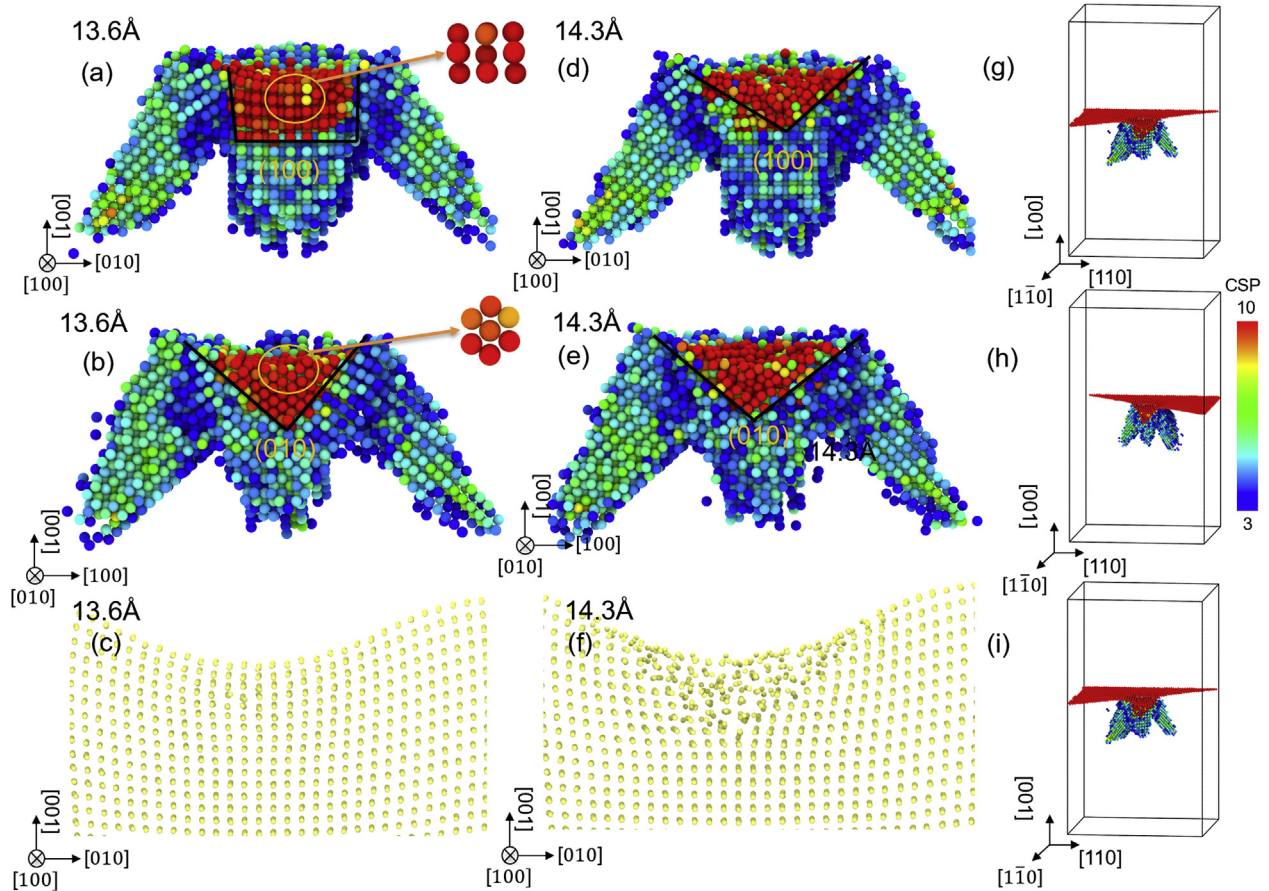


Fig. 9. (a–b) (100) and (010) sliced planes of $\delta\text{-ZrH}_2$ at an indenter depth of 13.6 Å during simulation for the [001] orientation (c) Thin slice of the H (100) plane in $\delta\text{-ZrH}_2$ at 13.6 Å, where H atoms are colored yellow and Zr atoms are hidden. (d–e) (100) and (010) sliced planes of $\delta\text{-ZrH}_2$ at a depth of 14.3 Å during simulation for the [001] orientation (f) Thin slice of the H (010) plane in $\delta\text{-ZrH}_2$ at 14.3 Å, where H atoms are colored yellow and Zr atoms are hidden. (g–i) The slice direction and which part we show for above figures. Atoms with CSP value < 3 and H atoms have been hidden in the (100) and (010) planes of $\delta\text{-ZrH}_2$. (For interpretation of the references to color in this figure legend, the reader is referred to the Web version of this article.)

coordination numbers and are more disordered. Comparing Fig. 9(e) to Figure 9(b), a different perspective of the same process as in panels (a) and (d), the atoms within the indicated triangle in (e) also become more disordered. The total number of atoms within the highly deformed region decreases, which is manifested as an inflection point in the total CSP value vs. indentation depth curve at depth 14.3 Å, as shown in Fig. 7(b). Comparison of Fig. 9(c) with (f) shows that at an indentation of 14.3 Å the H atoms also cannot maintain a simple cubic lattice and become disordered.

Fig. 10 shows snapshots of $\delta\text{-ZrH}_2$ at different indentation depths from three orientations. As shown in Fig. 10 (a)–(c), four $\{100\} <110>$ dislocations grow obliquely downwards beneath the xy-(001) surface. In addition, another dislocation grows under the lowest point of the contact area due to the compressive force directly from the indenter. This plastic deformation occurs in the highly deformed region, where all five dislocations start to nucleate, causing the dramatic load drop at the indentation of 13.6 Å. At an indentation depth of 14.3 Å, another four $\{100\} <110>$ dislocations are nucleated, releasing the internal stress inside the bulk ZrH_2 , making the load largely constant up to 16 Å. These dislocations are indicated by the yellow circles in Fig. 10 (e) and red arrows in Fig. 10(f). These dislocations grow just beneath and parallel to the surface of $\delta\text{-ZrH}_2$. In order to better illustrate these dislocations, the propagation directions of these fully formed $\{100\} <110>$ dislocations are indicated by red arrows in Fig. 11. The force continues to increase until 20 Å, at which there is a small plateau in

the load; at this load small $\{100\} <110>$ dislocations begin to nucleate as shown in the yellow circles in Figs. 10(i) and Figure 11, releasing some of the internal stress during deformation. In conclusion, before the first load drop, four $\{100\} <110>$ dislocations grow obliquely under the surface. After the first load drop, another four $\{100\} <110>$ dislocations begin to grow just beneath and parallel to the surface of the bulk ZrH_2 . There are also some small dislocations nucleated, as shown in the yellow circle of Fig. 11, which are not reflected as a load drop or plateau in the load-displacement curve during the nanoindentation.

4.2. Nanoindentation on (110) surface

We analyze the deformation during nanoindentation on the (110) surface in a similar manner to Section 4.1. Fig. 7(b) shows there is no clear load drop in the force vs. displacement curve; rather, the force gradually increases with indentation depth and the curve shape is narrower compared to the (100) surface. From Fig. 12(a)–(d), we see that the number of highly disordered atoms gradually increases with increasing indentation depth. Unlike the indentation on the (001) surface, the deformed region for the <011> orientation extends beneath the whole (011) xy surface. Also, as the red arrow shows in Fig. 12(d), the $\{100\} <011>$ dislocation gradually forms a spike just below the indenter. Fig. 12(e)–(f) shows that the $(01\bar{1})$ side plane of $\delta\text{-ZrH}_2$ is less disordered than the

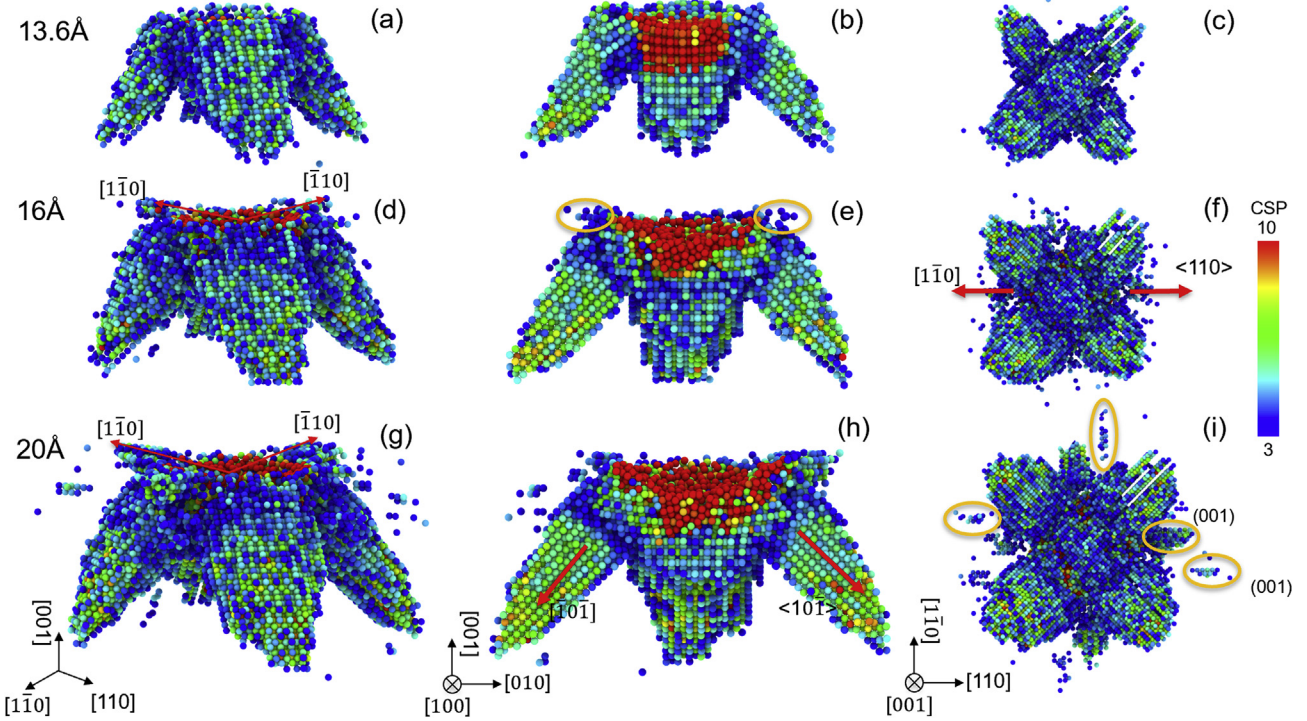


Fig. 10. Selected snapshots of δ -ZrH₂ at different indentation depths from a 3D perspective, a, d and g, side view, b, e and h, and top view, e, f, and i, during nanoindentation simulations for the [100] orientation. Atoms with CSP values < 3 and surface atoms have been hidden.

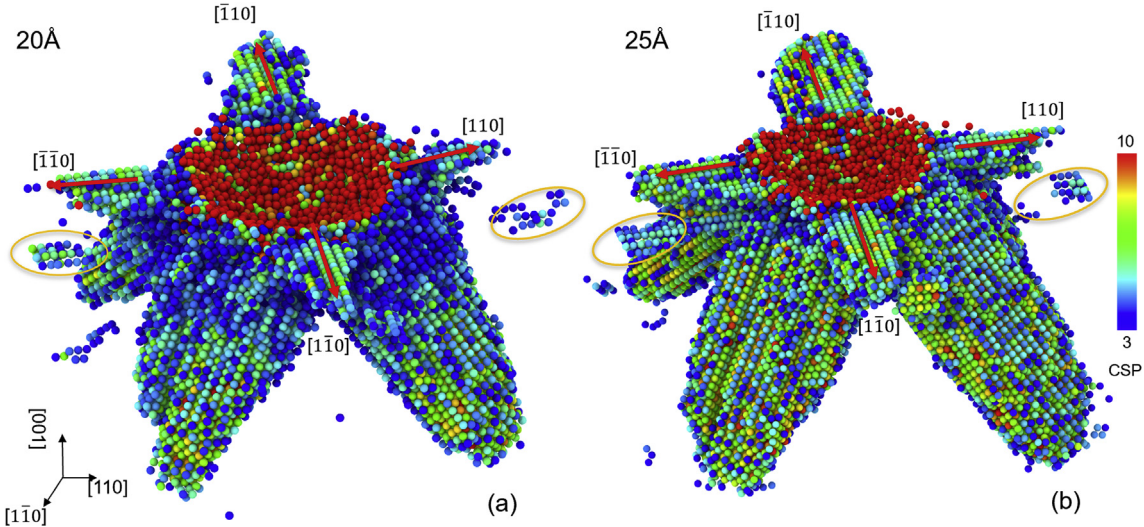


Fig. 11. Selected snapshots of δ -ZrH₂ at an indentation depth of 20 Å and 25 Å from a 3D perspective during nanoindentation simulations for the [100] orientation. Atoms with a CSP value < 3 and surface atoms have been hidden.

(100) side plane. The atoms forming the (01̄1) planes are mostly green, which means their CSP is smaller than the (100) plane and they are less disordered. This is because (100) plane can move along the <01̄1> direction, thereby reducing the atoms' asymmetry. However, inside the (100) plane, we see that two green regions form along the direction of the red arrows. These also show that the (010) plane slips along in the <01̄1> direction. Because the (010) <01̄1> dislocation and the (0̄10) <0̄11> dislocation move toward each other through the periodic boundary, these two dislocations inhibit each other's growth, causing the triangular region of

disordered atoms shown in Fig. 12(d–f).

During indentation, small dislocations grow along the <110> direction, as shown by red and yellow circles in Fig. 12(f). To further illustrate this, two snapshots at maximum indentation depths of 20 Å and 10 Å during unloading are shown in Fig. 12(g–h). Similar to the dislocations shown in Fig. 12(e–f), some small dislocations, indicated by red arrows in Fig. 12(g–h), grow along different [110] directions. Some (010) and (0̄10) planes, whose edges are shown on the (100) side plane as red lines extending to the surface, form an inverted triangle shape. These planes slip from one side of the <01̄1> direction, overcoming the resistance force dislocations on

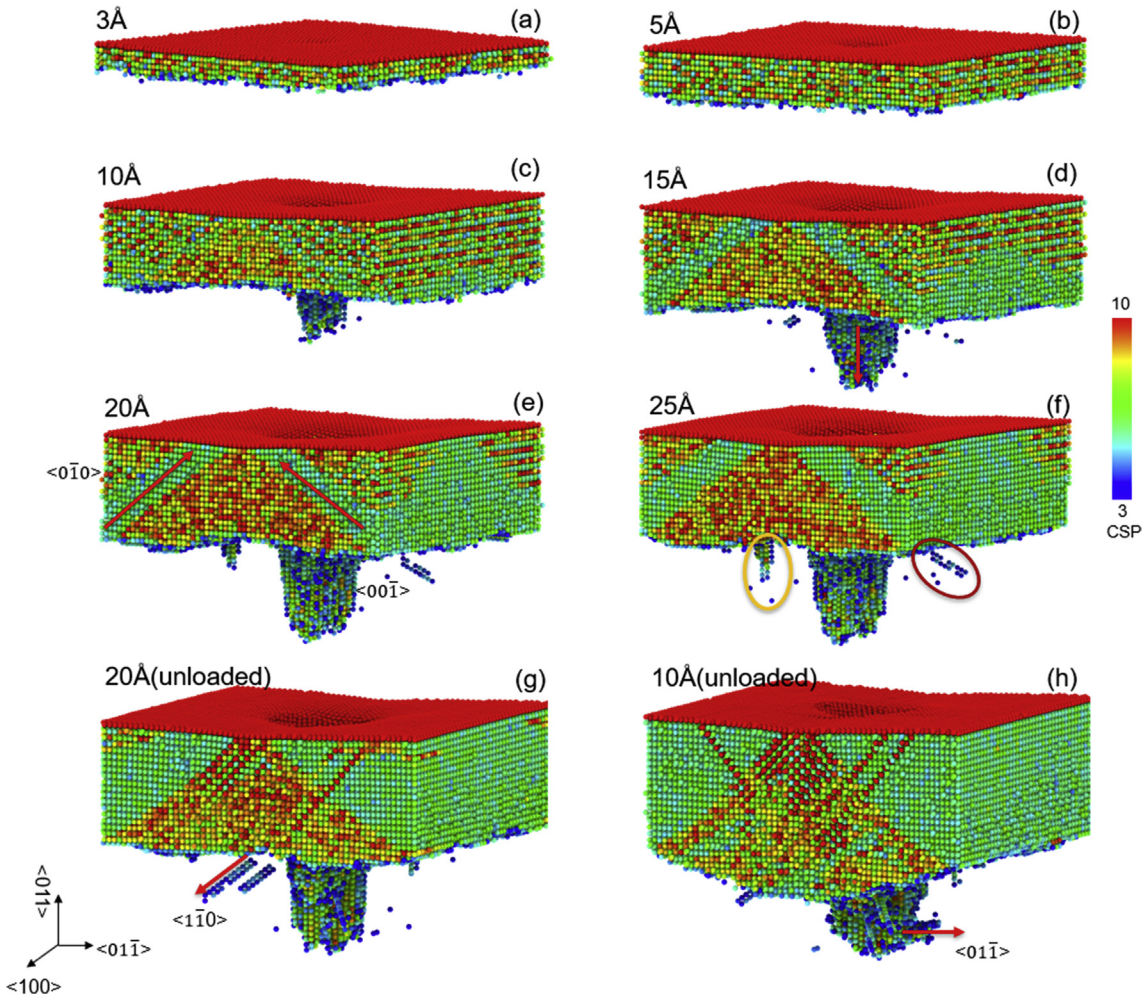


Fig. 12. The selected snapshots of $\delta\text{-ZrH}_2$ at different indentation depths from a 3D perspective during nanoindentation simulations for the [110] orientation. Atoms with a CSP value < 3 have been hidden.

the $(00\bar{1})$ plane, cross the center of the (100) side plane and become the red lines on the $[100]$ plane. Thus, Fig. 12(e–h) show one $(0\bar{1}1) < 0\bar{1}\bar{1}1 >$ and one $(010) < 01\bar{1} >$ dislocation growing on the (100) side plane and moving towards each other. Compared with Fig. 12(e–f), most of the disordered atoms in Fig. 12(g–h) are colored green, indicating weak disorder. During the unloading process, some dislocations recede and the degree of disorder at the upper corners on the (100) side plane reduces. However, the maximum depth of the center spike-shaped dislocation remains the same during the process.

The cross-sectional views of the (110) and (100) planes are shown in Fig. 13(a–b). It can be clearly seen in Fig. 13(a) that there is a distinct M-shape hollow surrounding the center spike dislocation. Because the atoms with a CSP value smaller than 3 are hidden, this hollow represents atoms with very low disorder; i.e., they are close to being on symmetric lattice sites. Atoms just beneath the indenter could either slip along the $<011>$ direction parallel to the page or along the $<011>$ direction following the movement of the indenter. Therefore, several different $\{100\}[100]$ dislocations grow from these atoms, which significantly decreases the amount of disorder and produces the hollow in Fig. 13(a–b). Another point of interest in Fig. 13(b) is that some Zr atoms, shown in the highly deformed region and marked by a yellow circle, change structure to AAA closed packing, whereas atoms in the spike dislocation region,

marked by a red circle, remain in an fcc structure. As in the case of the $[100]$ orientation, most hydrogen atoms remain in the simple cubic sublattice with only a few H atoms very close to the indenter becoming disordered.

5. Conclusions

Molecular dynamics simulations of nanoindentation on the (100) and (110) planes of $\delta\text{-ZrH}_2$ at 300 K are performed to investigate the deformation behavior and mechanisms using the COMB3 potential. It is found that the indenter speed doesn't have a significant influence on the indentation results. When the thickness of the active layer is small, the substrate effect is clear. The substrate effect becomes weaker with an increasing thickness of the active layer. The MD simulation results agree well with Hertz Law predictions in elastic region. While the calculated hardness from the indentation of the (100) and (110) surfaces of $\delta\text{-ZrH}_2$ are higher than the experimental values, the dimensionless load, (P/E^*) , and hardness, (H/E^*) , matches well with experiment. Yield behaviors are observed on the (100) surface but not on the (110) surface. In the highly deformed region, the Zr atom sublattice changes from an fcc structure to ABAB close packing during nanoindentation until the first load drop, while the H atom sublattice remains a simple cubic lattice due to the small atom size. The Zr and H atoms in the highly deformed region become totally disordered after the load

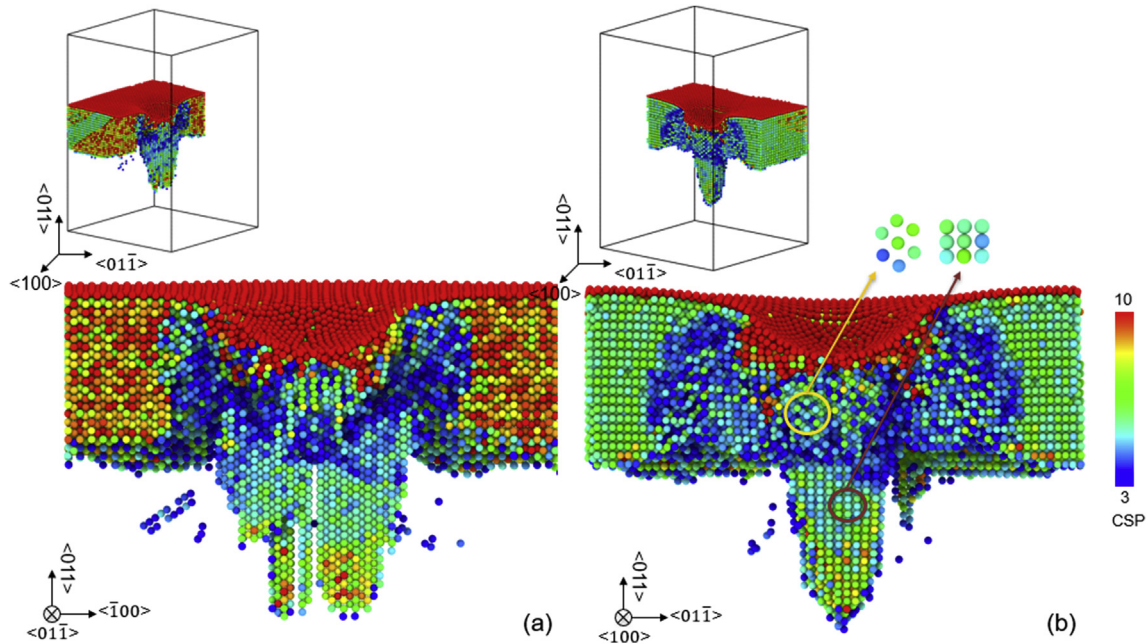


Fig. 13. Cross section of δ -ZrH₂ at an indentation depth of 25 Å during simulations for the [110] orientation. Atoms with a CSP value < 3 have been hidden.

drop for nanoindentation on the (100) plane. We find the dominant dislocation in the nanoindentation for both the (100) and (110) surfaces are {100} <110> dislocations. The newly nucleated dislocations grow parallel with the surface after yielding for indentation on the (100) surface with the increase of the depth. Small dislocations are also observed to nucleate and grow along the <110> directions with the increase of the indentation depth. In summary, we have clarified the deformation mechanism of δ -ZrH₂ under nanoindentation and described the factors that may influence the deformation, which not only strengthens the understanding of how zirconium hydrides result in zircaloy cladding failure but should also be helpful for developing the next generation of cladding.

Data availability statement

The data that support the findings of this study are available from the corresponding author upon reasonable request.

Author contributions

Linyuan Shi (石临源): Methodology, Software, Investigation, Writing - Original Draft, Visualization

Michele L. Fullarton: Assistance and discussion of research methods, potentials, and results. Writing - Review & Editing

Simon R. Phillpot: Conceptualization, Resources, Writing - Review & Editing, Supervision, Data curation

Declaration of competing interest

The authors declare that they have no known competing interests or personal relationships that could have appeared to influence the work reported in this paper.

References

- [1] A.T. Motta, A. Couet, R.J. Comstock, Corrosion of zirconium alloys used for nuclear fuel cladding, *Annu. Rev. Mater. Res.* 45 (2015) 311–343, <https://doi.org/10.1146/annurev-matsci-070214-020951>.
- [2] P. Chemelle, D.B. Knorr, J.B. Van Der Sande, R.M. Pelloux, M.A. Sande, P. Chemelle, et al., Morphology and composition of second phase particles in zircaloy-2, *J. Nucl. Mater.* 113 (1983) 58–64, [https://doi.org/10.1016/0022-3115\(83\)90166-6](https://doi.org/10.1016/0022-3115(83)90166-6).
- [3] H.K. Yueh, R.L. Kesterson, R.J. Comstock, H.H. Shah, D.J. Colburn, M. Dahlback, et al., Improved ZIRLO™ cladding performance through chemistry and process modifications, *Zircon. Nucl. Ind. Fourteenth Int. Symp.* (2005) 330–346, <https://doi.org/10.1520/STP37514S>.
- [4] N.A.P. Kiran Kumar, J.A. Szpunar, EBSD studies on microstructure and crystallographic orientation of δ -hydrides in Zircaloy-4, Zr-1% Nb and Zr-2.5% Nb, *Mater. Sci. Eng., A* 528 (2011) 6366–6374, <https://doi.org/10.1016/j.msea.2011.05.022>.
- [5] J.H. Kim, M.H. Lee, B.K. Choi, Y.H. Jeong, Effect of the hydrogen contents on the circumferential mechanical properties of zirconium alloy claddings, *J. Alloys Compd.* 431 (2007) 155–161, <https://doi.org/10.1016/j.jallcom.2006.05.074>.
- [6] Y.S. Kim, Temperature dependency of delayed hydride cracking velocity in Zr-2.5Nb tubes, *Mater. Sci. Eng., A* 468–470 (2007) 281–287, <https://doi.org/10.1016/j.msea.2006.09.123>.
- [7] P. Zhang, B. Wang, C. He, P. Zhang, First-principles study of ground state properties of ZrH₂, *Comput. Mater. Sci.* 50 (2011) 1–6, <https://doi.org/10.1016/j.commatsci.2011.06.016>.
- [8] C. Domain, R. Besson, A. Legris, Atomic-scale Ab-initio study of the Zr-H system: I. Bulk properties, *Acta Mater.* 50 (2002) 3513–3526, [https://doi.org/10.1016/S1359-6454\(02\)00173-8](https://doi.org/10.1016/S1359-6454(02)00173-8).
- [9] P.F. Weck, E. Kim, V. Tikare, J.A. Mitchell, Mechanical properties of zirconium alloys and zirconium hydrides predicted from density functional perturbation theory, *Dalton Trans.* 44 (2015) 18769–18779, <https://doi.org/10.1039/c5dt03403e>.
- [10] R.K. Siriprapu, B. Szpunar, J.A. Szpunar, Molecular dynamics study of hydrogen in α -zirconium, *Int J Nucl Energy* 2014 (2014) 1–6, <https://doi.org/10.1155/2014/912369>.
- [11] Z. Lu, M.J. Noordhoek, A. Chernatynskiy, S.B. Sinnott, S.R. Phillpot, Deformation processes in polycrystalline Zr by molecular dynamics simulations, *J. Nucl. Mater.* 462 (2015) 147–159, <https://doi.org/10.1016/j.jnucmat.2015.03.048>.
- [12] Z. Lu, A. Chernatynskiy, M.J. Noordhoek, S.B. Sinnott, S.R. Phillpot, Nano-indentation of Zr by molecular dynamics simulation, *J. Nucl. Mater.* 467 (2015) 742–757, <https://doi.org/10.1016/j.jnucmat.2015.10.042>.
- [13] Z. Lu, A. Chernatynskiy, M.J. Noordhoek, S.B. Sinnott, S.R. Phillpot, Nano-indentation of ZrO₂ and ZrO₂/Zr systems by molecular dynamics simulation, *J. Nucl. Mater.* 486 (2017) 250–266, <https://doi.org/10.1016/j.jnucmat.2017.01.022>.
- [14] J. Xu, S.Q. Shi, Investigation of mechanical properties of e-zirconium hydride using micro- and nano-indentation techniques, *J. Nucl. Mater.* 327 (2004) 165–170, <https://doi.org/10.1016/j.jnucmat.2004.02.004>.
- [15] S. Suman, M.K. Khan, M. Pathak, R.N. Singh, Investigation of elevated-temperature mechanical properties of δ -hydride precipitate in Zircaloy-4 fuel cladding tubes using nanoindentation, *J. Alloys Compd.* 726 (2017) 107–113, <https://doi.org/10.1016/j.jallcom.2017.07.321>.
- [16] A. Rico, M.A. Martin-Rengel, J. Ruiz-Hervias, J. Rodriguez, F.J. Gomez-Sanchez, Nanoindentation measurements of the mechanical properties of zirconium matrix and hydrides in unirradiated pre-hydrided nuclear fuel cladding,

- J. Nucl. Mater. 452 (2014) 69–76, <https://doi.org/10.1016/j.jnucmat.2014.04.045>.
- [17] Y. Li, A. Goyal, A. Chernatynskiy, J.S. Jayashankar, M.C. Kautzky, S.B. Sinnott, et al., Nanoindentation of gold and gold alloys by molecular dynamics simulation, Mater. Sci. Eng., A 651 (2016) 346–357, <https://doi.org/10.1016/j.msea.2015.10.081>.
- [18] T. Fu, X. Peng, C. Wan, Z. Lin, X. Chen, N. Hu, et al., Molecular dynamics simulation of plasticity in VN(001) crystals under nanoindentation with a spherical indenter, Appl. Surf. Sci. (2017), <https://doi.org/10.1016/j.japsusc.2016.09.130>.
- [19] S. Sun, X. Peng, H. Xiang, C. Huang, B. Yang, F. Gao, et al., Molecular dynamics simulation in single crystal 3C-SiC under nanoindentation: formation of prismatic loops, Ceram. Int. 43 (2017) 16313–16318, <https://doi.org/10.1016/j.ceramint.2017.09.003>.
- [20] L. Wang, H. Ke, J. Ma, J. Liu, Investigation of the ‘double cross’ splitting mechanism of single-crystal diamond under nanoindentation via molecular dynamics simulation, J. Mol. Model. 23 (2017) 299, <https://doi.org/10.1007/s00894-017-3467-9>.
- [21] M.I. Mendelev, G.J. Ackland, Development of an interatomic potential for the simulation of phase transformations in zirconium, Phil. Mag. Lett. 87 (2007) 349–359, <https://doi.org/10.1080/09500830701191393>.
- [22] M.J. Noordhoek, T. Liang, T.W. Chiang, S.B. Sinnott, S.R. Phillpot, Mechanisms of Zr surface corrosion determined via molecular dynamics simulations with charge-optimized many-body (COMB) potentials, J. Nucl. Mater. 452 (2014) 285–295, <https://doi.org/10.1016/j.jnucmat.2014.05.023>.
- [23] T. Liang, T.R. Shan, Y.T. Cheng, B.D. Devine, M.J. Noordhoek, Y. Li, et al., Classical atomistic simulations of surfaces and heterogeneous interfaces with the charge-optimized many-body (COMB) potentials, Mater. Sci. Eng. R Rep. 74 (2013) 255–279, <https://doi.org/10.1016/j.mser.2013.07.001>.
- [24] Y. Zhang, X.M. Bai, J. Yu, M.R. Tonks, M.J. Noordhoek, S.R. Phillpot, Homogeneous hydride formation path in α -Zr: molecular dynamics simulations with the charge-optimized many-body potential, Acta Mater. 111 (2016) 357–365, <https://doi.org/10.1016/j.actamat.2016.03.079>.
- [25] Y. Udagawa, M. Yamaguchi, H. Abe, N. Sekimura, T. Fuketa, Ab initio study on plane defects in zirconium-hydrogen solid solution and zirconium hydride, Acta Mater. 58 (2010) 3927–3938, <https://doi.org/10.1016/j.actamat.2010.03.034>.
- [26] T. Chihi, M. Fatmi, A. Bouhemadou, Structural, mechanical and electronic properties of transition metal hydrides MH 2 ($M = Ti, Zr, Hf, Sc, Y, La, v$ and Cr), Solid State Sci. 14 (2012) 583–586, <https://doi.org/10.1016/j.solidstatesciences.2012.02.010>.
- [27] S. Plimpton, Fast parallel algorithms for short-range molecular dynamics, J. Comput. Phys. 117 (1995) 1–19.
- [28] N. Grønbech-Jensen, Complete set of stochastic Verlet-type thermostats for correct Langevin simulations, Mol. Phys. (2019) 1–25, <https://doi.org/10.1080/00268976.2019.1662506>, 0.
- [29] T.H. Fang, C.I. Weng, J.G. Chang, Molecular dynamics analysis of temperature effects on nanoindentation measurement, Mater. Sci. Eng., A 357 (2003) 7–12, [https://doi.org/10.1016/S0921-5093\(03\)00219-3](https://doi.org/10.1016/S0921-5093(03)00219-3).
- [30] A. Stukowski, Visualization and analysis of atomistic simulation data with OVITO—the Open Visualization Tool, Model. Simulat. Mater. Sci. Eng. 18 (2010), 015012, <https://doi.org/10.1088/0965-0393/18/1/015012>.
- [31] A. Aladjem, Zirconium-hydrogen, Solid State Phenom. 49 (1996) 281–330.
- [32] K. Niki, G. Mochimaru, H. Shindo, Participation of {1 0 0} <0 1 1> slip system in sliding friction at (0 0 1), (1 1 0) and (1 1 0) surfaces of fluorite (CaF₂) crystal, Tribol. Online 7 (2012) 81–86, <https://doi.org/10.2474/trol.7.81>.
- [33] K.L. Johnson, K.L. Johnson, Contact Mechanics, Cambridge university press, 1987.
- [34] A.C. Fischer-Cripps, E.F. Gloyne, W.H. Hart, Introduction to Contact Mechanics, vol. 221, Springer, 2000.
- [35] M.J.P. Musgrave, Crystal Acoustics, Acoustical Society of America, New York, 2003.
- [36] A.G. Every, D.F. Nelson, K.-H. Hellwege, H. Landolt, R. Börnstein, O. Madelung, Crystal and Solid State Physics, Springer, 1992.
- [37] Z.A.D. Lethbridge, R.I. Walton, A.S.H. Marmier, C.W. Smith, K.E. Evans, Elastic anisotropy and extreme Poisson’s ratios in single crystals, Acta Mater. 58 (2010) 6444–6451.
- [38] A.N. Norris, Poisson’s ratio in cubic materials, Proc R Soc A Math Phys Eng Sci 462 (2006) 3385–3405.
- [39] C.L. Kelchner, S.J. Plimpton, J.C. Hamilton, Dislocation nucleation and defect structure during surface indentation, Phys. Rev. B 58 (1998) 11085–11088, <https://doi.org/10.1103/PhysRevB.58.11085>.
- [40] L.M. Keer, History of contact mechanics, in: Q.J. Wang, Y.-W. Chung (Eds.), Encycl. Tribol., Springer US, Boston, MA, 2013, pp. 1682–1684, https://doi.org/10.1007/978-0-387-92897-5_486.
- [41] C.A. Schuh, J.K. Mason, A.C. Lund, Quantitative insight into dislocation nucleation from high-temperature nanoindentation experiments, Nat. Mater. 4 (2005) 617–621, <https://doi.org/10.1038/nmat1429>.
- [42] A. Montagne, V. Audurier, C. Tromas, Influence of pre-existing dislocations on the pop-in phenomenon during nanoindentation in MgO, Acta Mater. 61 (2013) 4778–4786, <https://doi.org/10.1016/j.actamat.2013.05.004>.
- [43] S.R. Jian, C.H. Tasi, S.Y. Huang, C.W. Luo, Nanoindentation pop-in effects of Bi 2 Te 3 thermoelectric thin films, J. Alloys Compd. 622 (2015) 601–605, <https://doi.org/10.1016/j.jallcom.2014.10.133>.
- [44] C. Huang, X. Peng, T. Fu, X. Chen, H. Xiang, Q. Li, et al., Molecular dynamics simulation of BCC Ta with coherent twin boundaries under nanoindentation, Mater. Sci. Eng. A 700 (2017) 609–616, <https://doi.org/10.1016/j.msea.2017.06.048>.
- [45] A.M. Minor, S.A. Syed Asif, Z. Shan, E.A. Stach, E. Cyrankowski, T.J. Wyrobek, et al., A new view of the onset of plasticity during the nanoindentation of aluminium, Nat. Mater. 5 (2006) 697–702, <https://doi.org/10.1038/nmat1714>.
- [46] M. Piast, I. Kustrzeba-Wójcicka, M. Matusiewicz, T. Banaś, TRP subunits of anaphase-promoting complex mediate binding to the activator protein CDH1, Acta Biochim. Pol. 52 (2005) 507–513, <https://doi.org/10.1016/S0001-2013-0013-1>.
- [47] H. Xiang, H. Li, T. Fu, Y. Zhao, C. Huang, G. Zhang, et al., Molecular dynamics simulation of AlN thin films under nanoindentation, Ceram. Int. 43 (2017) 4068–4075, <https://doi.org/10.1016/j.ceramint.2016.11.218>.
- [48] T.Y. Tsui, G.M. Pharr, Substrate effects on nanoindentation mechanical property measurement of soft films on hard substrates, J. Mater. Res. 14 (1999) 292–301, <https://doi.org/10.1557/JMR.1999.0042>.
- [49] A.K. Nair, E. Parker, P. Gaudreau, D. Farkas, R.D. Kriz, Size effects in indentation response of thin films at the nanoscale: a molecular dynamics study, Int. J. Plast. 24 (2008) 2016–2031, <https://doi.org/10.1016/j.ijplas.2008.01.007>.
- [50] M. Nedim Cinbiz, M. Balooch, X. Hu, A. Amroussia, K. Terrani, Nanoindentation study of bulk zirconium hydrides at elevated temperatures, J. Alloys Compd. 726 (2017) 41–48, <https://doi.org/10.1016/j.jallcom.2017.07.319>.
- [51] M.L. Oyen, Nanoindentation hardness of mineralized tissues, J. Biomech. 39 (2006) 2699–2702, <https://doi.org/10.1016/j.jbiomech.2005.09.011>.
- [52] M.C. Chang, C.C. Ko, C.C. Liu, W.H. Douglas, R. DeLong, W.J. Seong, et al., Elasticity of alveolar bone near dental implant-bone interfaces after one month’s healing, J. Biomech. 36 (2003) 1209–1214, [https://doi.org/10.1016/S0021-9290\(03\)00113-1](https://doi.org/10.1016/S0021-9290(03)00113-1).
- [53] M.R. Maughan, D.F. Bahr, Dislocation activity under nanoscale contacts prior to discontinuous yield, Mater. Res. Lett. 3 (2014) 58–64, <https://doi.org/10.1080/21663831.2014.961663>.
- [54] J.D. Kiely, K.F. Jarausch, J.E. Houston, P.E. Russell, Initial stages of yield in nanoindentation, J. Mater. Res. 14 (1999) 2219–2227, <https://doi.org/10.1557/JMR.1999.0298>.
- [55] I. Salehinia, V. Perez, D.F. Bahr, Effect of vacancies on incipient plasticity during contact loading, Philos. Mag. A 92 (2012) 550–570, <https://doi.org/10.1080/14786435.2011.628635>.